Journal of CO2 Utilization 109 (2026) 103471

Contents lists available at ScienceDirect

Journal of CO2 Utilization

journal homepage: www.elsevier.com/locate/jcou

Synthesis of helical carbon nanofiber for greenhouse gas fixation and mechanistic insight into CO driven carbon formation

Atsuki Sakata [a], Hideki Abe [b], Takeshi Fujita [c], Akira Yamaguchi [a], Shigenori Ueda [b], Boborahimov Azamat Boborahim Ugli [b,d], Masahiro Miyauchi [a,*], Shusaku Shoji [b,*]

[a] Department of Materials Science and Engineering, School of Materials and Chemical Technology, Institute of Science Tokyo, 2-12-1 Ookayama, Meguro-ku, Tokyo 152-8552, Japan
[b] National Institute for Materials Science, 1-1 Namiki, Tsukuba, Ibaraki 304-0044, Japan
[c] School of Engineering Science, Kochi University of Technology, 185 Miyanokuchi, Tosayamada, Kami City, Kochi 782-8502, Japan
[d] Graduate School of Science and Engineering, Saitama University, Shimo-Okubo 255, Saitama 338-8570, Japan

A B S T R A C T

The utilization of carbon monoxide (CO), a key intermediate generated in CO_2 reduction and syngas-based processes, is a central challenge in carbon management. Although several studies have explored carbon growth from CO, conventional approaches often suffer from limited structural control and heterogeneous products, hindering the valorization of CO into advanced materials. Here, we report a robust and potentially scalable method to directly synthesize helical carbon nanofibers (hCNFs) from CO under ambient pressure, enabling a carbon-negative pathway when integrated with dry reforming of methane (DRM, $CH_4 + CO_2 \rightarrow 2\,H_2 + 2CO$). Using an earth-abundant Fe–Mo nanocomposite catalyst (Fe#MoO_x), we achieve uniform Fe nanoparticle stabilization during reduction and carburization, which is essential for controlled helical growth. The resulting hCNFs exhibit uniform morphology (≈100 nm diameter; several micrometers in length), a narrow diameter distribution ($\sigma < 11.6$ nm), high graphitic order, and a carbon yield of ~20% relative to carbon input. Notably, structural characterization reveals an exceptionally high density of edge-plane exposure, approaching the theoretical maximum attainable for CNFs. This feature endows the material with intrinsically high surface energy and provides a foundation for exploiting edge-rich carbon architectures in applications. In situ mass spectrometry and Raman spectroscopy further elucidate the distinct sequence of reduction, carburization, and spiral growth. By transforming CO into nanostructured carbons of unprecedented structural quality, this study provides a practical solution to the CO bottleneck in CO_2 utilization and establishes a platform for advanced applications in electrochemical storage, photothermal conversion, and biointerfaces.

1. Introduction

Carbon dioxide (CO_2) is considered a major greenhouse gas responsible for global warming. Consequently, substantial research has been devoted to reducing CO_2 emissions in key industrial sectors such as steelmaking, power generation, and cement manufacturing [1–3]. The Paris Agreement on climate change aims to limit the global temperature increase to well below 2 °C by imposing international obligations for net reductions in CO_2 emissions. Although technologies such as carbon capture and storage (CCS), which involve the direct underground sequestration of CO_2, are under active investigation to prevent its atmospheric release, numerous technical challenges remain, including issues related to long-term storage stability and potential leakage. [4,5].

In recent decades, various approaches have been researched to convert CO_2 into useful chemicals, including thermochemical, electrochemical, photocatalytic, and biological methods [6–9]. Among these, CO_2 hydrogenation — in which CO_2 reacts with H_2 to produce fuels or value-added chemicals via pathways such as methanation (Sabatier reaction), methanol synthesis, and the reverse water-gas shift (RWGS) reaction — has attracted particular attention as a scalable thermochemical route [10,11]. A promising extension of this concept is the conversion of CO_2-derived gases into solid carbon nanomaterials, which offers permanent carbon fixation while yielding high-value functional carbon products. However, these methods have not yet been widely implemented due to low reaction efficiency and generation of CO_2 during the process. To reduce the annual CO_2 emission of 40Gt, it is necessary to establish efficient, large-scale, and CO_2-neutral CO_2 fixation methods. [12,13].

Dry reforming of methane (DRM) is a highly promising method for CO_2 reduction. This reaction (chemical Eq. 1) enables the conversion of methane and CO_2 into mixture of hydrogen and carbon monoxide [14–19]. CH_4 and CO_2 are two of the top greenhouse gases, so the significance of converting them is immense.

Our previous work established a catalyst capable of maintaining

* Corresponding authors.
E-mail addresses: mmiyauchi@ceram.titech.ac.jp (M. Miyauchi), SHOJI.Shusaku@nims.go.jp (S. Shoji).

https://doi.org/10.1016/j.jcou.2026.103471
Received 29 September 2025; Received in revised form 3 May 2026; Accepted 20 May 2026
Available online 26 May 2026

stable activity for more than 1000 h, with no detectable side reactions such as coking. [20]. During this process, hydrogen is purified in high purity through a permeable membrane and is eliminated from the system. However, in systems represented by DRM, CO cannot be effectively utilized, leading to issues such as catalyst deactivation due to unexpected carbon deposition. If CO produced from greenhouse gases can be fixed in a useful form, it would have a significant impact on the environment, industry, and science.

Here, we report a method for producing carbon nanofibers (CNFs) with a uniform diameter from iron(Fe) and molybdenum (Mo) nanocomposites (Fe#MoO_x) using CO as raw material. These CNFs are helical in structure and feature highly exposed edge surface of carbon (hCNFs). Additionally, they exhibit strong hydrophilicity and disperse well in water. hCNFs are obtained by heating the Fe-Mo composite in a CO atmosphere. Typically, methods such as CVD process extracts carbon from CO to CNF(chemical Eqs. 2,3), but they are known to produce a lot of coarse and randomly formed carbon [21–23]. In contrast, our method utilizes a specific "Mo-pinning effect" to enforce a helical morphology even at mild temperatures (450 °C) under atmospheric pressure. Unlike conventional iron-catalyzed methods that often result in random carbon aggregates due to uncontrolled sintering, our Fe–Mo design regulates the nanoparticle size within a critical window, creating high-density active edges. This precise morphological control offers a distinct advantage over disordered carbons typically synthesized via the Boudouard reaction, providing a robust platform for solid carbon fixation.

$$CH_4 + CO_2 \rightarrow 2H_2 + 2CO \ \Delta H = +247\ kJ/mol \quad (1)$$

$$2CO \rightarrow C + CO_2 \ \Delta H = -172 kJ/mol \quad (2)$$

$$CO + H_2 \rightarrow C + H_2O \ \Delta H = -131 kJ/mol \quad (3)$$

Additionally, Reaction (1) is an endothermic reaction, while Reaction (2) is an exothermic reaction. Therefore, the most of reaction energy for (1) can be obtained by driving it with (2,3). By combining these two reactions, methane, a greenhouse gas, can be converted into high-value hCNF in a separate reaction environment without exhausting CO_2. Furthermore, this process simultaneously enables the extraction of hydrogen, which is essential for society. This makes it promising for applications in electrode materials, photothermal conversion materials, and biological applications. Furthermore, by upgrading CO into valuable solids of hCNF derived from greenhouse gases such as CH_4 and CO_2, our approach is expected to contribute to addressing environmental issues.

2. Experimental

2.1. Catalyst synthesis

A precursor plate of Fe-Mo alloy (Taiyo Koko Co.,LTD.) was sectioned into 6 mm × 6 mm squares and placed inside a quartz flow reactor, which was purged with argon gas. The gas was switched to a CO and O2 flow with a volumetric ratio of 2:1, and heat treatment was conducted at 600 °C for 12 h. The resulting plate (Fe#MoO_x) was used as a catalyst for subsequent carbon production.

2.2. Synthesis of hCNFs

The reactor was heated to 450 °C under the Ar atmosphere, after which a mixed gas containing 10% CO and 5% H_2 was introduced. The reaction was maintained for approximately 15 h. Preliminary tests with shorter (~5 h) and longer (20–25 h) durations revealed that ~15 h provided the optimum balance between yield and structural uniformity of the obtained hCNFs. The synthesis temperature of 450 °C was chosen based on preliminary screening in the 400–600 °C range, in which lower temperatures led to quite slow carbon growth rate and higher temperatures promoted random growth of carbon. The CO/H_2 composition (10%/5%) was selected to ensure both effective reduction/carburization of Fe to Fe_3C and suppression of excessive CO disproportionation, thereby yielding uniform helical CNFs. After the reaction, the reactor was cooled to room temperature under Ar atmosphere, and the sample was retrieved for subsequent analysis.

2.3. Characterization and measurement

A quadrupole mass spectrometer (QMS: Qulee BGM102, Ulvac) was used to continuously monitor the gas generated throughout the reaction in real time. The samples, both before and after the reaction, were characterized using X-ray diffraction (XRD: SmartLab, Rigaku), hard X-ray photoelectron spectroscopy (HAXPES), scanning electron microscopy (SEM: SU8230, Hitachi), scanning transmission electron microscopy (STEM: JEM-ARM200F NEOARM), and Raman spectroscopy (PR-1w, JASCO) to analyze structural, chemical, and morphological properties. For morphology analysis, SEM images were used to measure fiber diameters at 20 points across different regions of the sample. The average diameter and standard deviation were calculated as 96.4 nm, and a narrow size distribution ($\sigma < 11.6$ nm) was confirmed. Raman spectra were collected with a 532 nm laser, and the ID/IG ratio was calculated by fitting the D (~1350 cm^{-1}) and G (~1580 cm^{-1}) bands using Lorentzian functions, providing a measure of the graphitization degree and defect density of the synthesized hCNFs.

2.4. Performance evaluation

The adsorption performance was evaluated using Methylene Blue (MB) as a model pollutant. In a typical test, 20 mg of the adsorbent (hCNF, or benchmark materials including Multi Wall Carbon Nanotubes (MWCNTs), Activated Carbon, and Graphene) was dispersed in 10 mL of an aqueous MB solution with an initial concentration of 100 mg/L. The suspension was super sonicated then stirred continuously in the dark at room temperature to reach adsorption-desorption equilibrium. At predetermined time intervals, the carbon mixed solution were filtered to remove the adsorbent. The residual MB concentration was determined by measuring the absorbance at 664 nm using a UV–vis spectrophotometer. The adsorption capacity at 60 min (q_{60}) and surface utilization efficiency (ηSU) were calculated based on the mass balance principle and the specific surface area (S_{BET}) of each material.

The photothermal conversion capability was assessed using a solar simulator(ASAHI SPECTRA, HAL-320) equipped with an AM 1.5 G filter. The light intensity was calibrated to 100 mW/cm^2 (1 sun). The sample was then irradiated with simulated sunlight, and the surface temperature evolution was monitored in real-time using a radiative thermometer (JAPANSENSOR, FLHX-TNE). All measurements were conducted under ambient conditions.

3. Result and discussion

3.1. Morphology of hCNFs

Fig. 1 shows the SEM and STEM images of synthesized hCNFs. As shown in Fig. 1a, the carbon produced from Fe#MoO_x exhibits a helical structure. The synthesized hCNFs had a diameter of approximately 100 nm, a length of several micrometers, and a helical pitch of 250 nm, forming a continuous helical structure. All hCNFs obtained were uniform and exhibited consistent diameters(Fig. 1a). Furthermore, High resolution STEM analysis revealed that the hCNFs had a high exposure of edge planes(Fig. 1c, e and Figure S1). In contrast, carbon generated from iron metal, which is a typical catalyst for carbon production, under the same conditions was not observed to form fibers but instead grew in a random manner(Fig. 1b).Typically, in carbon nanotubes (CNTs), the basal planes of carbon are rolled up, leaving the edges unexposed [24–26]. In contrast, for graphene, the edges of its basal planes are exposed, representing high-energy sites where functional groups such as

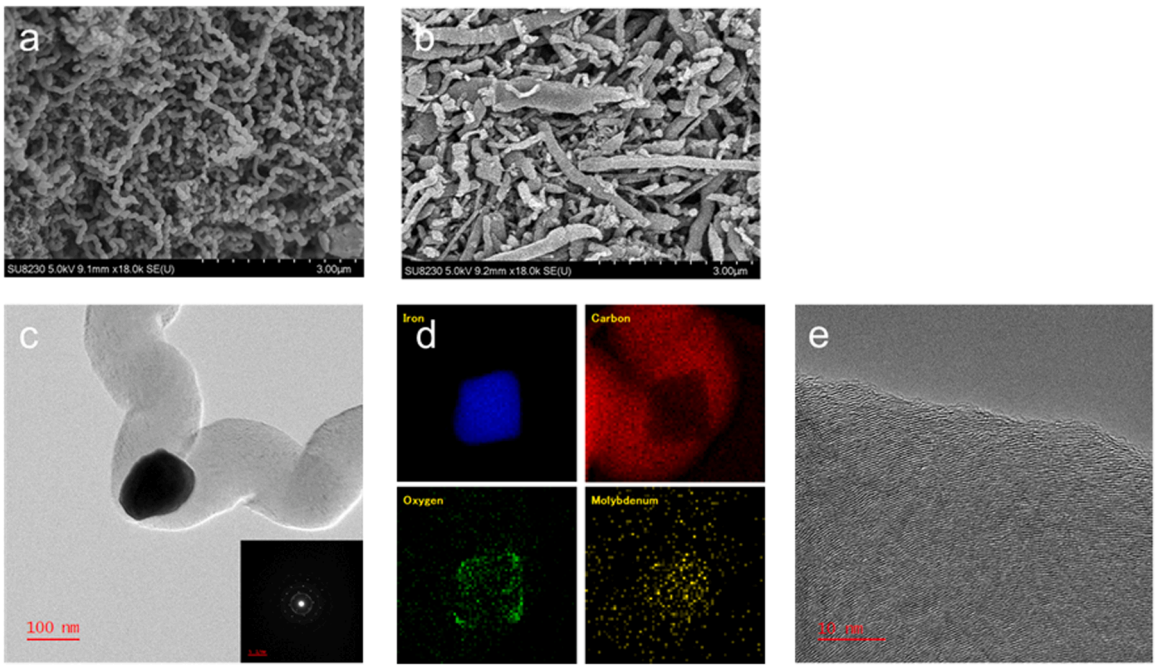

Figure. 1. SEM, TEM, and STEM-EDX images of synthesized carbon. (a)SEM image of hCNF from Fe#MoO_x precursor. (b)SEM image of amorphous carbon from Fe precursor. (c) TEM image of the tip of an hCNF and selected-area electron diffraction pattern. (d) STEM-EDX elemental maps of Fe, Mo and C acquired from the same region as panel (c), showing Fe in the particle core and Mo distributed at the periphery. (e) High-resolution STEM images of an hCNF, in which the exposed graphitic edges are clearly visible.

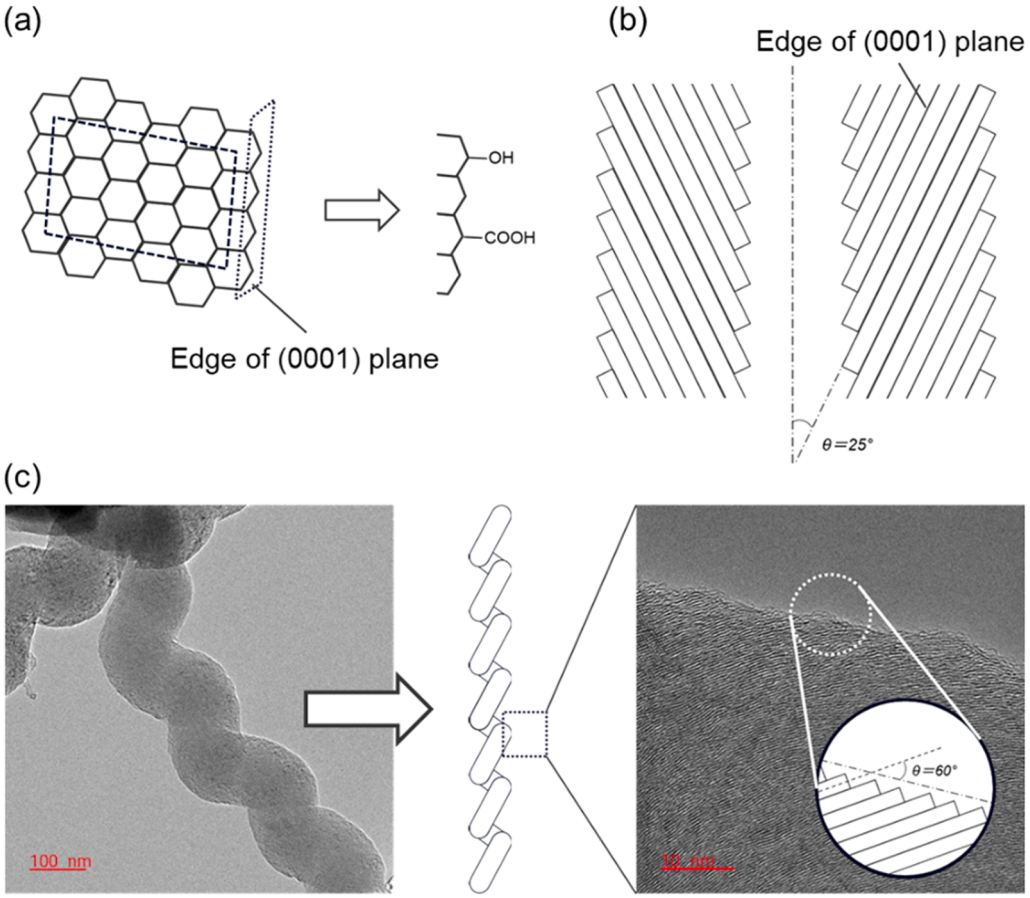

Figure. 2. Schematic diagrams of graphene(a) and commercially available CNFs with highly exposed edges (Pyrograf® from Aldrich), along with the STEM image and schematic diagram of hCNFs(c).

hydroxyl (OH) or carboxyl (COOH) groups are more likely to form [22,27,28](Fig. 2a). In our hCNFs, the helical structure facilitates significant exposure of these edge planes (0001), as evidenced by the analysis. Fig. 2b illustrates a schematic diagram of a commercially available CNF (Pyrograf®) that is generally recognized for having highly exposed edges. The angle θ between the outer peripheral surface and the edge planes of graphite is reported to be approximately 25°. Based on this, the number of edge planes per 10 nm, or the density of exposed edges, is calculated to be 14–20 edges per 10 nm. Theoretically, the edge density reaches 29.4 edges/10 nm when θ is 90°, as in the case of graphite.

In contrast, for hCNFs, θ is significantly larger at 60°, resulting in a calculated edge density of ~25 edges/10 nm(Fig. 2c). This corresponds to approximately 87% of the theoretical maximum edge density of ideal graphene edges. This geometric feature is critical for the enhanced surface activity discussed later. This indicates that the hCNFs exhibit an edge density several tens of percent higher than that of CNFs, which are generally considered to have highly exposed edges.

It is known that the size of CNFs varies depending on the size of the catalyst, when the size is a few nanometers, carbon nanotubes (CNTs) are formed, while at around 100 nm, helical CNFs are produced, and when the size exceeds that, random and coarse carbon fibers are more likely to form [29,30]. Fig. 3 shows the surface structure of Fe#MoO_x catalyst during the CO driven carbon formation reaction over time. By heating in a CO atmosphere, Fe-based particles are formed on the surface in the sequence of a → b → c, and after 4 h, it is observed that the Fe particles are being pushed up. It is revealed from the subsequent HAXPES measurements, described in the next section, that the Fe particles are in the form of cementite (Fe_3C)(FigureS2). During this process, the catalyst surface becomes homogenized in the range of 50–100 nm, and once the size of Fe_3C reaches this range, hCNFs are rapidly formed (Fig. 3d). In other words, the Fe#MoO_x catalyst promotes the formation of homogeneous Fe based nano-particles on the surface, and once these particles reach the optimal size, it functions as a substrate catalyst to generate uniform hCNFs. Furthermore, STEM-EDX analysis in Figure 1d reveals that Fe is concentrated in the nanoparticle core (consistent with the Fe_3C identified by XRD), while Mo is distributed mainly at the periphery of the particle and in the surrounding matrix, rather than at the apex from which carbon is extruded. This spatial segregation, combined with HAXPES analysis showing that Mo persists predominantly in a Mo^{4+} (MoO_2) oxidic state with only a minor surface-carbide contribution throughout the reaction (Figure S2) — in contrast to Fe, which is predominantly transformed to Fe_3C and Fe^0 as the operative phases for carbon growth (Figure S2; Fig. 4b) — supports the interpretation that Mo acts as a structural stabilizer at the Fe_3C surface rather than a direct catalytic site for CO dissociation, ensuring a narrow size distribution (50–100 nm) critical for hCNF growth. This size control prevents random carbon deposition and enables consistent helical morphology. [31] Our time-resolved analysis confirms that without Mo, Fe particles rapidly sinter into large aggregates (>200 nm), leading to amorphous carbon formation (Figure 1b). Thus, Mo acts as a critical structural stabilizer ("pinning agent") that confines Fe particles to the 50–100 nm window essential for helical growth. Under our standard conditions (10% CO + 5% H_2 in Ar, 50 sccm total flow, ~10 g Fe#MoO_x substrate, 450 °C, 15 h), approximately 20% of the supplied CO is converted to solid carbon — estimated by integration of the in-situ QMS CO and CO_2 traces (Fig. 5a) — corresponding to a carbon productivity of ≈ 24 mg_C per gram of bulk substrate over 15 h (≈ 1.6 mg_C g^{-1} h^{-1}). Because the catalytically active region is confined to the surface of the substrate, the per-gram-of-Fe productivity is considerably higher than this bulk-substrate value.

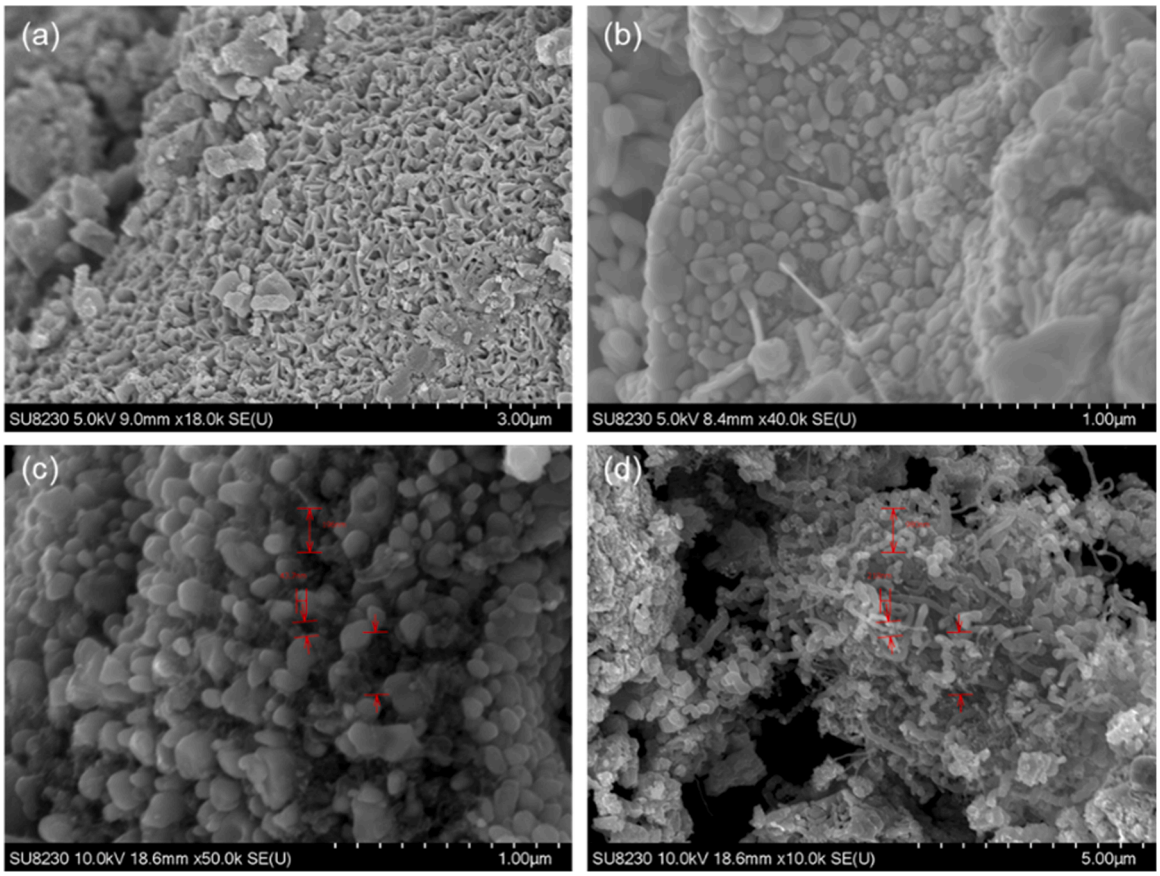

Fig. 3. SEM image of the substrate surface during the reaction(a)0 h (b)2 h (c)4 h (d)6 h.

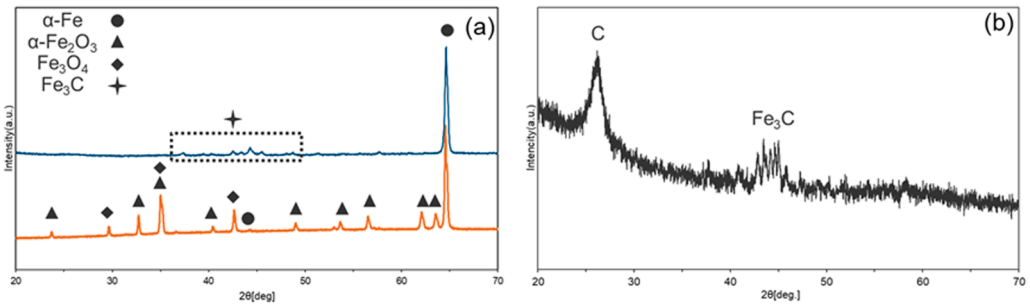

Fig. 4. (a) XRD patterns of Fe#MoO_x before the reaction (orange, bottom) and after the reaction (blue, top), showing the transition from Fe_2O_3/Fe to Fe_3C. (b) XRD pattern of the generated hCNFs separated from the Fe#MoOx substrate, displaying peaks of graphitic carbon and Fe_3C.

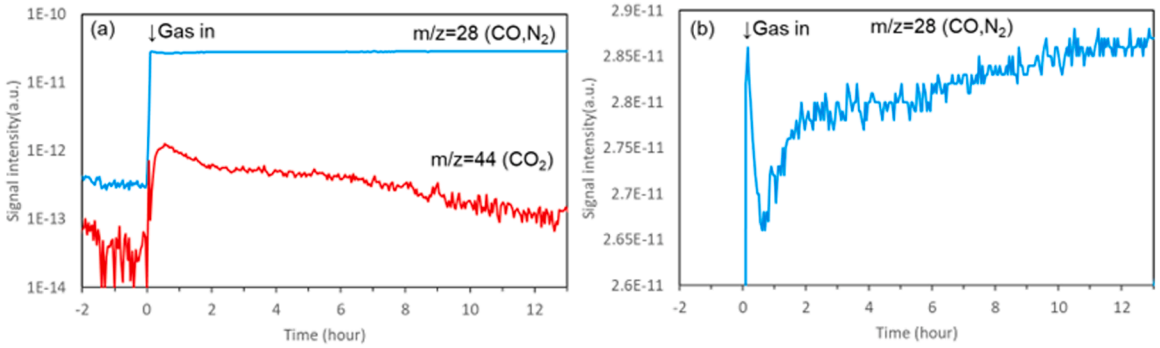

Fig. 5. (a) Temporal evolution of QMass signals of CO and CO_2 during the reaction. (b) Magnified view of the CO signal at the initial stage, highlighting its rapid consumption.

3.2. *Spectroscopic analysis of Fe#MoO_x and hCNF*

The HAXPES spectra(Figure S3) indicates that synthesized carbon exhibits peaks distinct from those of carbon nanotubes(CNTs), revealing the presence of a higher proportion of graphitic bonds [32,33]. This suggests that the synthesized carbon is closer to carbon nanofibers (CNFs) rather than CNTs. This result is good agreement with the STEM image, where the (0001) planes of graphite are stacked and exposed. HAXPES analysis of the Mo 3d region (Figure S2) confirms that Mo exists predominantly as Mo^{4+} (MoO_2; $3d_{5/2} \approx 229.5$ eV [34,35]) with a minor Mo^{6+} (MoO_3) contribution before the reaction, consistent with a mixed-valence surface-oxide environment. After the CO/H_2 treatment, the Mo 3d spectrum broadens, but Mo^{4+} remains the dominant component, with additional minor contributions from residual Mo^{6+} and a weak low-binding-energy shoulder near ~228 eV consistent with a small fraction of surface Mo^{2+} carbide [36]. Importantly, Mo does not undergo a clean transformation to a single reduced or carbide phase — in marked contrast to Fe, which is predominantly transformed to Fe_3C and Fe^0 as the operative phases for carbon growth confirmed by XRD of the separated hCNFs (Fig. 4b) and HAXPES(Figure S2). This chemical contrast supports the role of Mo as a structural stabilizer rather than an active carbon-growth site.

The XRD analysis prior to the reaction revealed that the main phase of Fe#MoO_x is a mixture of Fe_2O_3 and Fe (Fig. 4a, bottom). After the reaction, the main phase was identified as iron carbide (cementite, Fe_3C) (Fig. 4a, top). the strongest Fe peak observed at this stage originated from the bulk substrate, which did not participate in the reaction. In the hCNF grew on the surface, a strong peak attributed to carbon was observed near 26°, along with peaks corresponding to Fe_3C, whereas no peaks corresponding to metallic Fe were detected (Fig. 4b). This result is consistent with the STEM image and electron diffraction pattern of Fe_3C incorporated within the hCNF, as shown in Figure 1c.

The HAXPES analysis further confirmed the presence of Fe_3C even in the separated carbon generated on the surface of Fe#MoOx, indicating that Fe_3C generated from Fe#MoO_x served as the active site for hCNF growth(Figure S2). Previous studies have shown the same phenomenon, for example, hematite (iron oxide) being reduced to iron and subsequently carburized into cementite under a CO and H_2 atmosphere to produce carbon fibers [37–39]. Therefore, it can be inferred that a similar reaction is occurring in this case. It is worth noting that the residual Fe_3C cores impart magnetic properties to the hCNFs, allowing for easy magnetic separation in slurry-type applications such as water treatment. For applications where high carbon purity is strictly required (e.g., electrode materials), we confirmed that a simple acid treatment (e.g., aqua regia) can effectively remove the catalyst residues.

3.3. *Time resolved catalytic changes and hCNF growth*

Fig. 5 shows the temporal evolution of in-situ QMS signals throughout the reaction. From these data, qualitative changes in the concentrations of CO and CO_2 are clearly observed over time (Fig. 5a). In particular, during the initial stage of the reaction (Fig. 5b), a substantial decrease in the CO signal indicates that CO is rapidly consumed at the onset. Complementary in-situ Raman spectroscopy results (Figure S4) further reveal that carbon formation does not occur immediately but appears after a certain induction period following the introduction of CO and H_2 gases. Notably, the Raman spectra of the hCNFs show characteristic D and G bands at ~1350 and ~1580 cm^{-1} , respectively, with an intensity ratio ID/IG ≈ 2.96. This relatively high ratio indicates that, while the carbon possesses graphitic layers, it also contains a large number of edge sites and structural defects that strongly contribute to the D band intensity. This interpretation is consistent with the STEM observations, which clearly reveal graphitic stacking accompanied by abundant exposed edges. Thus, the carbon formed can be regarded as graphitic in nature but with a high density of edge-related defects, in line with the structural features observed in the microscopic analysis [40].

These observations suggest that, in the initial stage of the reaction, the reduction of iron oxide and its carburization into cementite take

Table 1
Comparison of adsorption performance and surface characteristics of hCNF and commercial carbon benchmarks.

Materials	Absorption Capacity $q_{60}(mg_{MB}/g_{carbons})$	BET surface area(m^2/g)	Surface Utilization Efficiency($mg_{MB}/m^2_{surface}$)
hCNF	32.3	46.05	0.701
MWCNTs	30.3	119.6	0.253
Activated Carbon	48.2	910.6	0.053
Graphene	45.1	8.16[a]	5.527[a]

Note: a The low surface area of graphene is attributed to sheet aggregation.

place. This reaction is consistent with those observed in direct reduction processes of iron under CO and H_2 atmospheres [37,38,41], with prior examples reported in the literature. The subsequent formation of carbon, following carburization, is corroborated by the changes observed in Raman spectra. Therefore, it can be concluded that the initial stage of the reaction involves the reduction and carburization of iron, while carbon formation occurs only after carburization has progressed to a certain extent.

When the gas was changed to CO only instead of CO + H_2, no carbon was generated, and XRD showed peaks corresponding to Fe_3O_4. This suggests that hydrogen plays a crucial role in the reduction of iron. Specifically, it indicates that it is necessary to reduce iron as a precursor to the transformation into Fe_3C. furthermore, after carbon formation, when the supply of H_2 gas was stopped and only CO was flowed, no CO_2 generation was observed. Similarly, this suggests that the presence of hydrogen is essential for the growth of carbon as well.

3.4. Adsorption performance and benchmarking

To evaluate the surface activity and industrial potential, we conducted Methylene Blue (MB) adsorption tests and compared the results with three representative benchmarks: Activated Carbon (AC), commercial Multi-Walled Carbon Nanotubes (MWCNTs), and Graphene Nanoplatelets. As summarized in Table 1, hCNF exhibited an equilibrium adsorption capacity (q_{60}) of 32.3 mg/g. Although this value is comparable to commercial MWCNTs (30.3 mg/g), the specific surface area of hCNF (46.1 m^2/g) is less than half that of MWCNTs (119.6 m^2/g). Consequently, the Surface Utilization Efficiency (η_{SU}) of hCNF is calculated to be 0.70 mg/m^2, which is ~2.8 times higher than that of MWCNTs (0.25 mg/m^2) and ~13 times higher than Activated Carbon (0.05 mg/m^2). This confirms that the hCNF surface is qualitatively superior (higher site density) compared to the basal-plane dominated walls of CNTs. Furthermore, in terms of kinetics (Figure S5), hCNF showed rapid adsorption comparable to AC in the initial stage, proving the excellent accessibility of the exposed helical edges. Notably, the experimental adsorption capacity of hCNF (38.4 mg/g) is approximately 82% of that of Graphene Nanoplatelets (46.6 mg/g, edge-rich reference). This ratio is in reasonable agreement with the geometric prediction derived in Section 3.1, where the edge density of hCNF was calculated to be ~87% of the theoretical maximum. This quantitative consistency supports the validity of our simplified helical model.

Additionally, regarding energy applications, we demonstrated the photothermal capability (Figure S6). The hCNF film exhibited a rapid temperature rise of 20 °C within 25 min under simulated sunlight, outperforming Graphene Nanoplatelets and MWCNTs due to enhanced light trapping within the helical structure. The superior photothermal heating of hCNFs can be well explained by their specific geometry, consistent with established light-trapping mechanisms. Similar to the multiple scattering effects reported in helical graphitic carbon nitrides, the coiled structure likely induces internal reflections that trap incident photons [42]. Additionally, the ~100 nm diameter suggests enhanced light absorption, likely due to multiple scattering and internal reflections within the helical structure, similar to light-trapping effects observed in other structured carbons. These precedents strongly indicate that the helical architecture effectively functions as a "light trap," resulting in the observed enhancement in photothermal conversion [43].

4. Conclusion

CO-based CNF synthesis typically results in random growth modes, yielding only coarse carbon. However, by using the Fe-Mo composite Fe#MoO_x, we successfully controlled carbon formation and synthesize high-quality hCNF. Through in-situ observations combining QMS gas analysis and Raman spectroscopy, we elucidated the reaction mechanism and identified the cause of carbon growth mode. In a H_2 and CO atmosphere, iron is reduced and carburized into iron carbide (cementite, Fe_3C), serving as the carbon source. The Fe–Mo nanocomposite (Fe#MoO_x) enabled uniform hCNF growth by controlling Fe nanoparticle size through Mo-assisted structural stabilization during reduction and carburization. This size control is essential because Fe particles outside the 50–100 nm range lead to CNT or amorphous carbon formation, whereas optimized Fe particle sizes favor helical CNF growth. Under standard conditions, the carbon productivity is ≈ 24 mg_C per gram of bulk Fe#MoO_x substrate over 15 h (CO conversion ≈ 20%, estimated from in-situ QMS). We note that the catalyst is single-use in its present form, since the active Fe nanoparticles become encapsulated into the growing hCNFs through a tip-growth mechanism; scalable industrial deployment will therefore require a regeneration or continuous-extraction strategy, which is a subject of ongoing work. Combining DRM with CO fixation is effective as it reduces greenhouse gases like methane and carbon dioxide while producing hydrogen. This study aims to achieve negative emissions of greenhouse gases and demonstrates the utility of greenhouse gas fixation technology through the synthesis of functional carbon.

CRediT authorship contribution statement

Boborahimov Azamat Boborahim Ugli: Data curation. **Masahiro Miyauchi:** Writing – review & editing, Supervision, Conceptualization. **Shusaku Shoji:** Writing – review & editing, Supervision, Conceptualization. **Hideki Abe:** Project administration, Conceptualization. **Takeshi Fujita:** Investigation, Formal analysis, Data curation. **Akira Yamaguchi:** Conceptualization. **Shigenori Ueda:** Investigation, Data curation. **Atsuki Sakata:** Writing – original draft, Investigation, Data curation.

Declaration of Competing Interest

The authors declare the following financial interests/personal relationships which may be considered as potential competing interests: Hideki Abe reports financial support was provided by New Energy and Industrial Technology Development Organization. If there are other authors, they declare that they have no known competing financial interests or personal relationships that could have appeared to influence the work reported in this paper.

Acknowledgements

This work was supported by the New Energy and Industrial Technology Development Organization (NEDO) under the Feasibility Study Program #23810887 and The Iketani Science and Technology

Foundation (Grant No. 0371200-A). We thank Taiyo Koko CO.,LTD. for providing us the samples. The synchrotron radiation experiments were performed at the BL09XU of SPring-8 with the approval of the Japan Synchrotron Radiation Research Institute (JASRI) (Proposal No. 2024A1536).

Content of Interest

- Demonstrates a robust and scalable method to directly synthesize high-quality helical carbon nanofibers (hCNFs) from CO, a key intermediate in CO_2 utilization and syngas chemistry.
- Integrates catalytic CO fixation with dry reforming of methane (DRM), providing a carbon-negative route to durable nanostructured carbon materials.
- Highlights a unique strategy to valorize CO_2-derived intermediates into high-value products, directly addressing the journal's focus on sustainable CO_2 conversion and utilization technologies.
- Offers industrial relevance by coupling greenhouse-gas mitigation with the scalable production of advanced carbon nanomaterials.

Appendix A. Supporting information

Supplementary data associated with this article can be found in the online version at doi:10.1016/j.jcou.2026.103471.

Data availability

Data will be made available on request.

References

[1] D.I. Armstrong McKay, A. Staal, J.F. Abrams, R. Winkelmann, B. Sakschewski, S. Loriani, et al., Exceeding 1.5°C global warming could trigger multiple climate tipping points, Science 377 (6611) (2022 Sep 9) eabn7950, https://doi.org/10.1126/science.abn7950.

[2] K. Anderson, G. Peters, The trouble with negative emissions, Science 354 (6309) (2016) 182.

[3] H.D. Matthews, S. Wynes, Current global efforts are insufficient to limit warming to 1.5°C, Science 376 (6600) (2022 Jun 24) 1404–1409, https://doi.org/10.1126/science.abo3378.

[4] Q. Deng, X. Ling, K. Zhang, L. Tan, G. Qi, J. Zhang, CCS and CCUS technologies: giving the oil and gas industry a green future, Front Energy Res 10 (2022 Jun 17) 919330, https://doi.org/10.3389/fenrg.2022.919330.

[5] S. Chen, J. Liu, Q. Zhang, F. Teng, B.C. McLellan, A critical review on deployment planning and risk analysis of carbon capture, utilization, and storage (CCUS) toward carbon neutrality, Renew. Sustain Energy Rev. 167 (2022 Oct 1) 112537, https://doi.org/10.1016/j.rser.2022.112537.

[6] Y. Yuan, E. Huang, S. Hwang, P. Liu, J.G. Chen, Converting carbon dioxide into carbon nanotubes by reacting with ethane, Angew. Chem. Int Ed. 136 (2024) e202404047.

[7] Z. Xie, E. Huang, S. Garg, S. Hwang, P. Liu, J.G. Chen, CO2 fixation into carbon nanofibres using electrochemical–thermochemical tandem catalysis, Nat. Catal. 7 (1) (2024 Jan 1) 98–109, https://doi.org/10.1038/s41929-023-01085-1.

[8] H. Yu, E. Haviv, R. Neumann, Visible light photochemical reduction of CO2 to CO coupled to hydrocarbon dehydrogenation, Angew. Chem. Int Ed. 132 (15) (2020) 6278.

[9] F.M. Schwarz, J. Moon, F. Oswald, V. Müller, Biological hydrogen storage and release through multiple cycles of bi-directional hydrogenation of CO2 to formic acid in a single process unit, Joule 6 (6) (2022 Jun) 1304–1319, https://doi.org/10.1016/j.joule.2022.04.020.

[10] C. Guo, Y. Tang, Z. Yang, T. Zhao, J. Liu, Y. Zhao, et al., Reinforcing the efficiency of photothermal catalytic CO_2 methanation through integration of Ru nanoparticles with photothermal $MnCo_2O_4$ nanosheets, ACS Nano 17 (23) (2023 Dec 12) 23761–23771, https://doi.org/10.1021/acsnano.3c07630.

[11] J. Wang, J. Wang, J. Feng, Y. Hu, H. Huang, N. Zhang, et al., Photochemical CO2 hydrogenation to carbon nanotubes and H2O for oxygen recovery in space exploration, Joule 8 (11) (2024 Nov) 3126–3141, https://doi.org/10.1016/j.joule.2024.08.007.

[12] Committee on Developing a Research Agenda for Carbon Dioxide Removal and Reliable Sequestration, Board on Atmospheric Sciences and Climate, Board on Energy and Environmental Systems, Board on Agriculture and Natural Resources, Board on Earth Sciences and Resources, Board on Chemical Sciences and Technology, et al., Negative Emissions Technologies and Reliable Sequestration: A Research Agenda [Internet], National Academies Press, Washington, D.C, 2019. ⟨https://www.nap.edu/catalog/25259⟩ [cited 2025 Mar 12]. Available from.

[13] S. Zhang, Y. Shen, C. Zheng, Q. Xu, Y. Sun, M. Huang, et al., Recent advances, challenges, and perspectives on carbon capture, Front Environ. Sci. Eng. 18 (6) (2024 Jun) 75, https://doi.org/10.1007/s11783-024-1835-0.

[14] B. Agún, A. Abánades, Comprehensive review on dry reforming of methane: Challenges and potential for greenhouse gas mitigation, Int J. Hydrog. Energy 103 (2025 Feb) 395–414, https://doi.org/10.1016/j.ijhydene.2025.01.160.

[15] Z. Alipour, V. Babu Borugadda, H. Wang, A.K. Dalai, Syngas Production through Dry Reforming: A Review on Catalysts and Their Materials, Preparation Methods and Reactor Type, Chem. Eng. J. 452 (2023) 139416.

[16] X. Chen, Z. Sheng, S. Murata, S. Zen, H.H. Kim, T. Nozaki, CH4 dry reforming in fluidized-bed plasma reactor enabling enhanced plasma-catalyst coupling, J. CO2 Util. 54 (2021) 101771.

[17] H. Kaneko, Y. Cho, T. Sugimura, A. Hashimoto, A. Yamaguchi, M. Miyauchi, Sustaining syngas production at a near-unity H_2 /CO ratio in the photo-induced dry reforming of methane independent of the reactant gas composition, Chem. Commun. 60 (75) (2024) 10406–10409, https://doi.org/10.1039/D4CC03088E.

[18] Y. Cho, S. Shoji, A. Yamaguchi, T. Hoshina, T. Fujita, H. Abe, et al., Visible-light-driven dry reforming of methane using a semiconductor-supported catalyst, Chem. Commun. 56 (33) (2020) 4611–4614, https://doi.org/10.1039/D0CC00729C.

[19] H. Jiao, G.C. Wang, A Comprehensive theoretical study of the mechanism for dry reforming of methane on a Ni4/ZrO2(101) catalyst under external electric fields: the role of interface and oxygen vacancy, ACS Catal. 15 (5) (2025 Mar 7) 3846–3859, https://doi.org/10.1021/acscatal.4c05758.

[20] S. Shoji, X. Peng, T. Imai, P.S. Murphin Kumar, K. Higuchi, Y. Yamamoto, et al., Topologically immobilized catalysis centre for long-term stable carbon dioxide reforming of methane, Chem. Sci. 10 (13) (2019) 3701–3705, https://doi.org/10.1039/C8SC04965C.

[21] V.S. Gangoli, M.A. Godwin, G. Reddy, R.K. Bradley, A.R. Barron, The State of HiPco Single-Walled Carbon Nanotubes in 2019, C 5 (4) (2019 Oct 28) 65, https://doi.org/10.3390/c5040065.

[22] I.Y. Jeon, H.J. Choi, S.M. Jung, J.M. Seo, M.J. Kim, L. Dai, et al., Large-scale production of edge-selectively functionalized graphene nanoplatelets via ball milling and their use as metal-free electrocatalysts for oxygen reduction reaction, J. Am. Chem. Soc. 135 (4) (2013 Jan 30) 1386–1393, https://doi.org/10.1021/ja3091643.

[23] M.S. Saravanan, S.P. Babu, K. Sivaprasad, M. Jagannatham, Techno-economics of carbon nanotubes produced by open air arc discharge method, Int J. Eng. Sci. Technol. 2 (5) (2010 Sep 28) 100–108, https://doi.org/10.4314/ijest.v2i5.60128.

[24] N. Gupta, S.M. Gupta, S.K. Sharma, Carbon nanotubes: synthesis, properties and engineering applications, Carbon Lett. 29 (5) (2019 Oct) 419–447, https://doi.org/10.1007/s42823-019-00068-2.

[25] W. Fan, L. Zhang, T. Liu, Structures and Properties of Carbon Nanomaterials. Graphene-Carbon Nanotube Hybrids for Energy and Environmental Applications [Internet], Springer Singapore, Singapore, 2017, pp. 1–19, https://doi.org/10.1007/978-981-10-2803-8_1 [cited 2025 Mar 12].

[26] Z. Jiang, N.N. Intan, Q. Yang, *Ab initio* insight into the electrolysis of water on basal and edge (fullerene C_{20}) surfaces of 4 Å single-walled carbon nanotubes, RSC Adv. 12 (52) (2022) 33552–33558, https://doi.org/10.1039/D2RA06123F.

[27] A. Cassidy, S. Pedersen, H. Bluhm, V. Calisti, T. Angot, E. Salomon, et al., Patterned formation of enolate functional groups on the graphene basal plane, Phys. Chem. Chem. Phys. 20 (45) (2018) 28370–28374, https://doi.org/10.1039/C8CP05730C.

[28] S.V. Pavlov, S.A. Kislenko, Graphene electrochemistry: edge vs. basal plane sites, J. Phys. Conf. Ser. 1092 (2018 Sep) 012112, https://doi.org/10.1088/1742-6596/1092/1/012112.

[29] D. Li, L. Pan, Y. Wu, W. Peng, The effect of changes in synthesis temperature and acetylene supply on the morphology of carbon nanocoils, Carbon 50 (7) (2012 Jun) 2571–2580, https://doi.org/10.1016/j.carbon.2012.02.015.

[30] X. Jian, M. Jiang, Z. Zhou, Q. Zeng, J. Lu, D. Wang, et al., Gas-Induced Formation of Cu Nanoparticle as Catalyst for High-Purity Straight and Helical Carbon Nanofibers, ACS Nano 6 (10) (2012 Oct 23) 8611–8619, https://doi.org/10.1021/nn301880w.

[31] S. Panic, B. Bajac, S. Rakić, Á. Kukovecz, Z. Kónya, V. Srdić, et al., Molybdenum anchoring effect in Fe–Mo/MgO catalyst for multiwalled carbon nanotube synthesis, React. Kinet. Mech. Catal. 122 (2) (2017 Dec) 775–791, https://doi.org/10.1007/s11144-017-1291-y.

[32] D. Sengupta, S.H. Chen, A. Michael, C.Y. Kwok, S. Lim, Y. Pei, et al., Single and bundled carbon nanofibers as ultralightweight and flexible piezoresistive sensors, npj Flex. Electron 4 (1) (2020 May 20) 9, https://doi.org/10.1038/s41528-020-0072-2.

[33] T.I.T. Okpalugo, P. Papakonstantinou, H. Murphy, J. McLaughlin, N.M.D. Brown, High resolution XPS characterization of chemical functionalised MWCNTs and SWCNTs, Carbon 43 (1) (2005) 153–161, https://doi.org/10.1016/j.carbon.2004.08.033.

[34] D.O. Scanlon, G.W. Watson, D.J. Payne, G.R. Atkinson, R.G. Egdell, D.S.L. Law, Theoretical and experimental study of the electronic structures of MoO3 and MoO2, J. Phys. Chem. C. 114 (10) (2010) 4636–4645, https://doi.org/10.1021/jp9093172.

[35] J. Baltrusaitis, B. Mendoza-Sanchez, V. Fernandez, R. Veenstra, N. Dukstiene, A. Roberts, et al., Generalized molybdenum oxide surface chemical state XPS determination via informed amorphous sample model, Appl. Surf. Sci. 326 (2015) 151–161, https://doi.org/10.1016/j.apsusc.2014.11.077.

[36] C. Wan, Y.N. Regmi, B.M. Leonard, Multiple phases of molybdenum carbide as electrocatalysts for the hydrogen evolution reaction, Angew. Chem. Int Ed. 53 (25) (2014) 6407–6410, https://doi.org/10.1002/anie.201402998.

[37] M.L. Ali, Q. Fradet, U. Riedel, Kinetic mechanism development for the direct reduction of single hematite pellets in H_2 /CO atmospheres, Steel Res Int 93 (12) (2022 Dec) 2200043, https://doi.org/10.1002/srin.202200043.
[38] N. Towhidi, J. Szekely, The influence of carbon deposition on the reduction kinetics of commercial grade hematite pellets with CO, H_2, and N_2, Met. Trans. B 14 (1983) 359–367, https://doi.org/10.1007/BF02654354.
[39] T.K.S. Kumar, J. Alatalo, H. Ahmed, B. Björkman, Effect of temperature and gas mixtures on cementite formation during the carburization of hydrogen-reduced DRI, J. Sustain Met. 8 (4) (2022 Dec) 1450–1464, https://doi.org/10.1007/s40831-022-00601-0.
[40] C. Casiraghi, A. Hartschuh, H. Qian, S. Piscanec, C. Georgi, A. Fasoli, et al., Raman spectroscopy of graphene edges, Nano Lett. 9 (4) (2009 Apr 8) 1433–1441, https://doi.org/10.1021/nl8032697.
[41] E.T. Turkdogan, J.V. Vinters, Gaseous reduction of iron oxides: part I. Reduction of hematite in hydrogen, Met. Trans. 2 (11) (1971 Nov) 3175–3188, https://doi.org/10.1007/BF02814970.
[42] Y. Zheng, L. Lin, X. Ye, F. Guo, X. Wang, Helical graphitic carbon nitrides with photocatalytic and optical activities, Angew. Chem. Int Ed. 53 (44) (2014 Oct 27) 11926–11930.
[43] J.K. Gansel, M. Thiel, M.S. Rill, M. Decker, K. Bade, V. Saile, et al., Gold helix photonic metamaterial as broadband circular polarizer, Science 325 (5947) (2009 Sept 18) 1513–1515.